Available online at www.sciencedirect.com
ScienceDirect
Journal of Computational Physics 227 (2008) 7952–7976
JOURNAL OF COMPUTATIONAL PHYSICS
www.elsevier.com/locate/jcp

Improving shock irregularities based on the characteristics of the MHD equations

Tomoyuki Hanawa [a,*], Hayato Mikami [b], Tomoaki Matsumoto [c]

[a] *Center for Frontier Science, Chiba University, Yayoi-cho 1-33, Chiba 263-8522, Japan*
[b] *Graduate School of Science, Chiba University, Yayoi-cho 1-33, Chiba 263-8522, Japan*
[c] *Department of Humanity and Environment, Hosei University, Fujimi, Chiyoda-ku, Tokyo 102-8160, Japan*

Received 26 April 2007; received in revised form 4 April 2008; accepted 7 May 2008
Available online 23 May 2008

Abstract

We have developed a numerical simulation scheme for three-dimensional magnetohydrodynamical flow with shocks. The numerical scheme is based on the Roe-type scheme and includes additional numerical diffusion in the direction tangential to the shock front to care the carbuncle instability. The numerical viscosity is added only in the regions where the characteristics of either fast or slow wave converges, i.e., in the regions potentially dangerous to the carbuncle instability. Accordingly the numerical viscosity is as small as that of the Roe scheme except near the shock fronts. It is demonstrated from comparison with the HLLE scheme that the magnetic Reynolds number is higher in the simulations obtained with our scheme. We show application of the scheme to the magnetohydrodynamical simulations of type II supernova. It is also proved that the scheme is free from the odd–even decoupling.
© 2008 Elsevier Inc. All rights reserved.

PACS: 47.11.–j

Keywords: Carbuncle phenomenon; Shock instability; Numerical shock structure; Magnetohydrodynamics; Riemann solvers; Upwind schemes

1. Introduction

The carbuncle instability is notorious by serious damages to shock waves. It produces unphysical bumps near shock fronts in multi-dimensional hydrodynamical simulations. Since the discovery of the carbuncle phenomenon by Peery and Imlay [1], many schemes have been examined. Shock capturing schemes such as Roe's [2] flux difference splitting (FDS) scheme suffer from the carbuncle instability seriously. A less diffusive scheme is sensitive to the carbuncle instability as pointed out by Quirk [3]. The carbuncle instability is so complex that the emergence depends not only on evaluation of numerical flux but also on many factors including initial

* Corresponding author. Tel.: +81 43 290 3525; fax: +81 43 290 3523.
E-mail address: hanawa@cfs.chiba-u.ac.jp (T. Hanawa).

0021-9991/$ - see front matter © 2008 Elsevier Inc. All rights reserved.
doi:10.1016/j.jcp.2008.05.006

condition (see, e.g., [4]). Since the mechanism of carbuncle instability has not been fully understood yet, proposed cures are derived either phenomenologically or heuristically. No scheme has been proved to be free from the carbuncle instability.

In practical simulations we choose a scheme by considering both artificial diffusion due to numerical viscosity and vulnerability to the carbuncle instability. A sensible scheme should be less diffusive and free from the carbuncle instability. However, no good choice has bee known for solving the magnetohydrodynamical (MHD) equations. Although HLLE [5,6] is less sensitive to the carbuncle instability, the numerical viscosity is large. Most of the known cures are designed for solving the hydrodynamical equations and cannot be directly applied to MHD.

In this paper we propose a numerical scheme for the MHD equations. The scheme provides a carbuncle free solution while the numerical viscosity is smaller than that of HLLE. Our approach is similar to those of Wada and Liou [7] and of Kim et al. [8] and based on the Quirk's [3] strategy. First we identify the shock fronts since the nearby regions are potentially dangerous to the carbuncle instability. The identification is based on the spatial variation of the characteristics and is similar to that by Wada and Liou [7]. We supplement additional numerical viscosity to the Roe-type scheme there. The additional viscosity diffuses disturbances in the directions tangential to the shock fronts. As well as Liou [9], we use the spatial distribution of characteristic speed to design the additional viscosity. It is designed to be larger where the shock is stronger.

This paper is organized as follows. Section 2 describes the scheme and Section 3 shows its application to the odd–even decoupling problem. Section 4 shows application to type II supernova in which expanding spherical shock waves and bipolar outflows emerge. Section 5 discusses the validity of our numerical viscosity.

2. Numerical scheme

2.1. Basic equations

We consider the ideal magnetohydrodynamical (MHD) equations in the Cartesian coordinates. They are expressed as

$$\frac{\mathrm{d}\boldsymbol{U}}{\partial t}+\frac{\mathrm{d}\boldsymbol{F}_x}{\partial x}+\frac{\mathrm{d}\boldsymbol{F}_y}{\partial y}+\frac{\mathrm{d}\boldsymbol{F}_z}{\partial z}=0, \tag{1}$$

$$\boldsymbol{U}=\begin{pmatrix}\rho\\ \rho v_x\\ \rho v_y\\ \rho v_z\\ B_x\\ B_y\\ B_z\\ \rho E\end{pmatrix},\qquad \boldsymbol{F}_x=\begin{pmatrix}\rho v_x\\ \rho v_x^2+P+\frac{\boldsymbol{B}^2}{8\pi}-\frac{B_x^2}{4\pi}\\ \rho v_x v_y-\frac{B_xB_y}{4\pi}\\ \rho v_x v_z-\frac{B_xB_z}{4\pi}\\ 0\\ v_xB_y-v_yB_x\\ v_xB_z-v_zB_x\\ \rho H v_x-\frac{\boldsymbol{v}\cdot\boldsymbol{B}}{4\pi}B_x\end{pmatrix}, \tag{2}$$

$$\boldsymbol{F}_y=\begin{pmatrix}\rho v_y\\ \rho v_y v_x-\frac{B_yB_x}{4\pi}\\ \rho v_y^2+P+\frac{\boldsymbol{B}^2}{8\pi}-\frac{B_y^2}{4\pi}\\ \rho v_y v_z-\frac{B_yB_z}{4\pi}\\ v_xB_y-v_yB_x\\ 0\\ v_zB_y-v_yB_z\\ \rho H v_y-\frac{\boldsymbol{v}\cdot\boldsymbol{B}}{4\pi}B_y\end{pmatrix},\qquad \boldsymbol{F}_z=\begin{pmatrix}\rho v_z\\ \rho v_z v_x-\frac{B_zB_x}{4\pi}\\ \rho v_z v_y-\frac{B_zB_y}{4\pi}\\ \rho v_x^2+P+\frac{\boldsymbol{B}^2}{8\pi}-\frac{B_x^2}{4\pi}\\ v_xB_z-v_zB_x\\ v_yB_z-v_zB_y\\ 0\\ \rho H v_z-\frac{\boldsymbol{v}\cdot\boldsymbol{B}}{4\pi}B_z\end{pmatrix}, \tag{3}$$

$$E = \frac{\boldsymbol{v}^2}{2} + \varepsilon + \frac{\boldsymbol{B}^2}{8\pi\rho}, \tag{4}$$

and

$$H = E + \frac{P}{\rho} + \frac{\boldsymbol{B}^2}{8\pi\rho}. \tag{5}$$

The symbols, ρ and P, denote the density and pressure. The vectors, $\boldsymbol{v} = (v_x, v_y, v_z)$ and $\boldsymbol{B} = (B_x, B_y, B_z)$, denote the velocity and magnetic field, respectively. The symbols, E and H, denote the specific energy and specific enthalpy, respectively. The symbol, ε, denotes the specific internal energy.

The characteristics of the MHD equations are evaluated from the Jacobi matrices, $(\partial \boldsymbol{F}_x/\partial \boldsymbol{U})$, $(\partial \boldsymbol{F}_y/\partial \boldsymbol{U})$, and $(\partial \boldsymbol{F}_z/\partial \boldsymbol{U})$ as shown by Brio and Wu [10]. The characteristic speeds propagating in the x-direction are expressed as

$$\lambda_x^{(1)} = v_x + c_{f,x}, \tag{6}$$
$$\lambda_x^{(2)} = v_x + b_x, \tag{7}$$
$$\lambda_x^{(3)} = v_x + c_{s,x}, \tag{8}$$
$$\lambda_x^{(4)} = v_x, \tag{9}$$
$$\lambda_x^{(5)} = v_x - c_{s,x}, \tag{10}$$
$$\lambda_x^{(6)} = v_x - b_x, \tag{11}$$
$$\lambda_x^{(7)} = v_x - c_{f,x}, \tag{12}$$

where

$$(c_f)^2 = \frac{(a_*)^2 + \sqrt{(a_*)^4 - 4(ab_x)^2}}{2}, \tag{13}$$
$$(c_s)^2 = \frac{(a_*)^2 - \sqrt{(a_*)^4 - 4(ab_x)^2}}{2}, \tag{14}$$
$$a^2 = \left(\frac{\partial P}{\partial \rho}\right)_s, \tag{15}$$
$$(a_*)^2 = a^2 + (b_x)^2 + (b_y)^2 + (b_z)^2, \tag{16}$$
$$b_x = \frac{|B_x|}{\sqrt{4\pi\rho}}, \tag{17}$$
$$b_y = \frac{|B_y|}{\sqrt{4\pi\rho}}, \tag{18}$$
$$b_z = \frac{|B_z|}{\sqrt{4\pi\rho}}. \tag{19}$$

The symbols, a, denotes the adiabatic sound speed. The symbols, $c_{f,x}$ and $c_{s,x}$, denote the phase velocities of the fast and slow magnetohydrodynamical waves, respectively. The symbols, b_x, b_y, and b_z, denote the Alfvén speeds in the x-, y-, and z-directions, respectively. The characteristic speeds are numbered in the decreasing order so that,

$$\lambda_x^{(k)} \geqslant \lambda_x^{(k+1)} \tag{20}$$

for any k.

2.2. Identification of the shock front

Carbuncle instability takes place only in the regions close to shock fronts. The shock fronts are identified by the pressure difference between adjacent cells in Kim et al. [8]. The pressure difference is indeed a good measure of the shock strength in hydrodynamics. However, it may not be in magnetohydrodynamics (MHD), since magnetic force may dominate over the pressure force. Alternatively, we select regions potentially dangerous to the carbuncle instability from the spatial change in the characteristic speed according to Wada and Liou [7]. They identified the shock front from the change in the characteristic speed of sound waves. MHD flows contain four types of waves, the fast, slow, Alfvén and entropy waves, which propagate at the characteristic speeds. The former two steepen and evolve into shock waves. Thus we measure steepening of them by the following procedures.

First we compute the characteristic speeds of MHD waves propagating in the x-direction at each cell. They are numbered in the decreasing order as

$$\lambda^{(1)}_{x,i,j,k} = v_{x,i,j,k} + c_{f,i,j,k}, \tag{21}$$

$$\lambda^{(2)}_{x,i,j,k} = v_{x,i,j,k} + b_{x,i,j,k}, \tag{22}$$

$$\lambda^{(3)}_{x,i,j,k} = v_{x,i,j,k} + c_{s,i,j,k}, \tag{23}$$

$$\lambda^{(4)}_{x,i,j,k} = v_{x,i,j,k}, \tag{24}$$

$$\lambda^{(5)}_{x,i,j,k} = v_{x,i,j,k} - c_{s,i,j,k}, \tag{25}$$

$$\lambda^{(6)}_{x,i,j,k} = v_{x,i,j,k} - b_{x,i,j,k}, \tag{26}$$

$$\lambda^{(7)}_{x,i,j,k} = v_{x,i,j,k} - c_{f,i,j,k}. \tag{27}$$

where the subscripts, i, j, and k denote the cell position in the x-, y-, and z-directions, respectively. The maximum characteristic speed, $\lambda^{(1)}_{x,i,j,k}$, denotes the characteristic speed of the fast wave propagating rightward in the x-direction, while the minimum one, $\lambda^{(7)}_{x,i,j,k}$, does that propagating leftward. When and only when $\lambda^{(1)}_{x,i,j,k} > \lambda^{(1)}_{x,i+1,j,k}$, the fast wave propagating rightward steepens and will evolve into the shock wave eventually. Similarly the fast wave propagating leftward steepens when and only when $\lambda^{(7)}_{x,i,j,k} > \lambda^{(7)}_{x,i+1,j,k}$. Thus the spatial difference in the characteristic speed denotes rate of wave compression and gives us a measure of wave steepening. Similarly when and only when $\lambda^{(3)}_{x,i,j,k} > \lambda^{(3)}_{x,i+1,j,k}$ or $\lambda^{(5)}_{x,i,j,k} > \lambda^{(5)}_{x,i+1,j,k}$, the slow waves evolve into the shock waves. In short, the spatial difference in the characteristic speed is an indicator for shock wave. For later convenience, we define the index,

$$\Delta\lambda_{x,i+1/2,j,k} \equiv \max(\Delta\lambda^{(1)}_{x,i+1/2,j,k}, \Delta\lambda^{(3)}_{x,i+1/2,j,k}, \Delta\lambda^{(5)}_{x,i+1/2,j,k}, \Delta\lambda^{(7)}_{x,i+1/2,j,k}), \tag{28}$$

where

$$\Delta\lambda^{(1)}_{x,i+1/2,j,k} = \max(\lambda^{(1)}_{x,i,j,k} - \lambda^{(1)}_{x,i+1,j,k}, 0), \tag{29}$$

$$\Delta\lambda^{(3)}_{x,i+1/2,j,k} = \max(\lambda^{(3)}_{x,i,j,k} - \lambda^{(3)}_{x,i+1,j,k}, 0), \tag{30}$$

$$\Delta\lambda^{(5)}_{x,i+1/2,j,k} = \max(\lambda^{(5)}_{x,i,j,k} - \lambda^{(5)}_{x,i+1,j,k}, 0), \tag{31}$$

$$\Delta\lambda^{(7)}_{x,i+1/2,j,k} = \max(\lambda^{(7)}_{x,i,j,k} - \lambda^{(7)}_{x,i+1,j,k}, 0). \tag{32}$$

When the index, $\Delta\lambda_{x,i+1/2,j,k}$, is positive and large, the cell surface is close to the shock front. The shock is stronger when the index is larger.

When $\Delta\lambda_{x,i+1/2,j,k}$ is positive, the cells, (i,j,k) and $(i+1,j,k)$, may suffer from the carbuncle instability. Thus we need supplement numerical viscosity to the fluxes flowing through the cell surfaces, $(i,j-1/2,k)$, $(i,j+1/2,k)$, $(i+1,j-1/2,k)$, $(i+1,j+1/2,k)$, $(i,j,k-1/2)$, $(i,j,k+1/2)$, $(i+1,j,k-1/2)$, and $(i+1,j,k+1/2)$ in order to avoid the carbuncle instability [8,9].

The argument mentioned above is illustrated in Fig. 1, in which the lines denote the cell surfaces in the two dimension. When the cell surface denoted by the solid line has a positive index, $\Delta\lambda_{x,i+1/2,j,k}$, the cells marked D

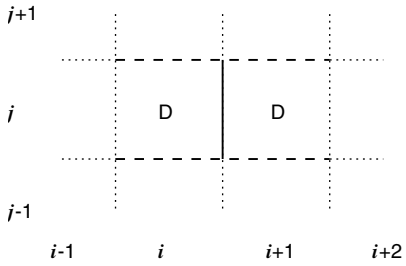

Fig. 1. The cells marked D are potentially dangerous to the carbuncle instability, when the index is positive on the cell surface denoted by the thick solid line. An additional numerical viscosity is added to the fluxes on the cell surfaces denoted by the dashed lines.

are potentially dangerous to the carbuncle instability. The carbuncle instability will be erased out by diffusion if numerical viscosity is enhanced for the cell surfaces denoted by the dashed lines.

2.3. Numerical viscosity

First we examine the numerical viscosity of the original Roe scheme. In the original Roe scheme, the first order accurate solution is expressed as

$$\boldsymbol{U}_{i,j,k}^{(n+1)} = \boldsymbol{U}_{i,j,k}^{(n)} - \Delta t \times \left[\frac{\boldsymbol{F}_{x,i+1/2,j,k}^{(\mathrm{ROE})} - \boldsymbol{F}_{x,i-1/2,j,k}^{(\mathrm{ROE})}}{\Delta x} + \frac{\boldsymbol{F}_{y,i,j+1/2,k}^{(\mathrm{ROE})} - \boldsymbol{F}_{y,i,j+1/2,k}^{(\mathrm{ROE})}}{\Delta y} + \frac{\boldsymbol{F}_{z,i,j,k+1/2}^{(\mathrm{ROE})} - \boldsymbol{F}_{z,i,j,k-1/2}^{(\mathrm{ROE})}}{\Delta z} \right], \tag{33}$$

where $\boldsymbol{F}_{x,i\pm1/2,j,k}^{(\mathrm{ROE})}$, $\boldsymbol{F}_{y,i,j\pm1/2,k}^{(\mathrm{ROE})}$, and $\boldsymbol{F}_{z,i,j,k\pm1/2}^{(\mathrm{ROE})}$ denote the numerical fluxes evaluated at the cell surfaces normal to the x-, y- and z-directions, respectively. The subscripts specify the cells and surfaces in which the conservative variable and numerical flux are evaluated. The numerical flux is expressed as

$$\boldsymbol{F}_{i+1/2,j,k}^{(\mathrm{ROE})} = \frac{\boldsymbol{F}_{i,j,k} + \boldsymbol{F}_{i+1,j,k}}{2} - \frac{1}{2} \sum_{m=1}^{7} \mid \lambda_{x,i+1/2,j,k}^{(m)} \mid \delta w_m \boldsymbol{r}_m, \tag{34}$$

where δw_m and $\boldsymbol{r}_m$ denote the mth wave amplitude and eigen vector, respectively. They are chosen to satisfy the property U so that both

$$\boldsymbol{U}_{j+1} - \boldsymbol{U}_j = \sum_{m=1}^{7} \delta w_m \boldsymbol{r}_m, \tag{35}$$

and

$$\boldsymbol{F}_{x,j+1} - \boldsymbol{F}_{x,j} = \sum_{m=1}^{7} \lambda_{x,i+1/2,j,k}^{(m)} \delta w_m \boldsymbol{r}_m, \tag{36}$$

hold simultaneously. The explicit form of $\lambda^{(m)}$, $\boldsymbol{r}_m$, and δw_m was obtained by Cargo and Gallice [11] for the ideal gas having a constant specific heat ratio. It is extended for a non-ideal gas by Hanawa et al. [12].

We can evaluate the numerical viscosity of the Roe scheme from Eq. (34). The second term in the right hand side denotes the diffusive flux. The dynamical viscosity is $|\lambda_{x,i+1/2,j,k}^{(m)}|\Delta x$ for the mth wave. If we replace $\mid \lambda_{x,i+1/2,j,k}^{(m)} \mid$ with a lager one, then we obtain a more diffusive numerical flux.

We employ a larger numerical viscosity to avoid both the expansion shock and carbuncle instability. The former is removed by employing the entropy fix to the fast and slow waves. We replace $|\lambda_{x,i+1/2,j,k}^{(m)}|$ in the right hand side of Eq. (34) with the maximum of $|\lambda_{x,i,j,k}^{(m)}|$ and $|\lambda_{x,i+1,j,k}^{(m)}|$ for $m = 1, 3, 5$, and 7 when $\lambda_{x,i,j,k}^{m} < 0$ and $\lambda_{x,i+1,j,k}^{m} > 0$ simultaneously.

Our care for the carbuncle instability is designed with the following observations on HLLE scheme in mind. The simple version of HLLE takes account of only maximum and minimum characteristic speeds. It seems to be resistant to the carbuncle although it suffers from 1D carbuncle instability [4]. This suggests two things; (1) we need not employ a viscosity larger than that of HLLE scheme and (2) no additional numerical viscosity is

likely to be necessary for the fast waves. The index, $\Delta\lambda_{x,i+1/2,j,k}$, has the dimension of velocity and is a reasonable candidate for the numerical viscosity for the Alfvén and slow waves. The entropy wave is the most sensitive to the carbuncle instability as pointed out by Liou [9]. Thus the numerical viscosity should be larger for the entropy wave.

On the basis of the above argument, we propose a numerical flux defined as

$$\boldsymbol{F}^*_{x,i+1/2,j,k} = \frac{\boldsymbol{F}_{x,i,j,k} + \boldsymbol{F}_{x,i+1,j,k}}{2} - \frac{1}{2}\sum_{k=1}^{N} \Lambda^{(m)}_{x,i+1/2,j,k}\delta w_m \boldsymbol{r}_m, \tag{37}$$

where $\Lambda^{(m)}$ denotes the numerical viscosity in the unit of velocity. It is taken to be

$$\Lambda^{(m)}_{x,i+1/2,j,k} = \mid \lambda^{(m)}_{x,i+1/2,j,k} \mid \tag{38}$$

for the fast wave ($m = 1$ and 7). In other words, no additional numerical viscosity is supplemented to the Roe flux. It is taken to be

$$\Lambda^{(m)}_{x,i+1/2,j,k} = \max(\mid \lambda^{(m)}_{x,i+1/2,j,k} \mid, \Delta\tilde{\lambda}_{x,i+1/2,j,k}), \tag{39}$$

$$\Delta\tilde{\lambda}_{x,i+1/2,j,k} \equiv \max(\Delta\lambda_{y,i,j-1/2,k}, \Delta\lambda_{y,i,j+1/2,k}, \Delta\lambda_{y,i+1,j-1/2,k}, \Delta\lambda_{y,i+1,j+1/2,k}, \Delta\lambda_{z,i,j,k-1/2}, \Delta\lambda_{z,i,j,k+1/2}, \Delta\lambda_{z,i+1,j,k-1/2}, \Delta\lambda_{z,i+1,j,k+1/2}) \tag{40}$$

for the Alfvén ($m = 2$ and 6) and slow ($m = 3$ and 5) waves so that the numerical viscosity is increased according to the shock indicator. For the entropy wave ($m = 4$), the numerical viscosity is set equal to that of HLLE,

$$\Lambda^{(4)}_{x,i+1/2,j,k} = (\lambda^{(1)}_{x,i+1/2,j,k} - \lambda^{(7)}_{x,i+1/2,j,k})^{-1} |(\lambda^{(1)}_{x,i+1/2,j,k} + \lambda^{(7)}_{x,i+1/2,j,k})\lambda^{(4)}_{x,i+1/2,j,k} - 2\lambda^{(1)}_{x,i+1/2,j,k}\lambda^{(7)}_{x,i+1/2,j,k}|, \tag{41}$$

in the regions where $\Delta\lambda_{x,i+1/2,j,k} > 0$. It is set equal to that in the Roe flux,

$$\Lambda^{(4)}_{x,i+1/2,j,k} = \mid \lambda^{(4)}_{x,i+1/2,j,k} \mid, \tag{42}$$

in the rest regions, where $\Delta\lambda_{x,i+1/2,j,k} = 0$ [see, Eqs. (29)–(32)]. Note that Eq. (40) cares all the cases in which either the cell (i, j, k) or $(i + 1, j, k)$ may suffer from the carbuncle instability.

Eq. (39) means that the wave propagation speed, $\mid \lambda^{(m)}_{x,i+1/2,j,k} \mid$, is the threshold for the numerical viscosity in the sense that the numerical viscosity is increased only when the shock indicator exceeds the threshold. On the other hand, Eq. (42) sets no threshold for the viscosity applied to the entropy wave. This means that the numerical viscosity is supplemented even if wave steepening is very weak and the region is unlikely to be vulnerable to the carbuncle instability. The overabundant numerical viscosity may be suppressed by setting an appropriate threshold, although we have not yet investigated the possibility.

Similarly we can obtain the numerical flux, $\boldsymbol{F}_{y,i,j+1/2,k}$ and $\boldsymbol{F}_{z,i,j,k+1/2}$. With these modified numerical flux, we obtain the first order accurate solution,

$$\boldsymbol{U}^{(n+1)}_{i,j,k} = \boldsymbol{U}^{(n)}_{i,j,k} - \Delta t \times \left[\frac{\boldsymbol{F}^*_{x,i+1/2,j,k} - \boldsymbol{F}^*_{x,i-1/2,j,k}}{\Delta x} + \frac{\boldsymbol{F}^*_{y,i,j+1/2,k} - \boldsymbol{F}^*_{y,i,j+1/2,k}}{\Delta y} + \frac{\boldsymbol{F}^*_{z,i,j,k+1/2} - \boldsymbol{F}^*_{z,i,j,k-1/2}}{\Delta z}\right]. \tag{43}$$

The numerical flux given by Eq. (37) is of the first order accurate in space. The second order accurate solution is obtained with the aid of MUSCL (Monotone Upstream-centered Schemes for Conservation Law, see e.g., Hirsch [13]). The examples shown in the subsequent sections are second order accurate both in space and in time.

Since we evaluate all the physical quantities at the cell center, the solution has $\nabla \cdot \boldsymbol{B}$ of numerical origin. We employed the method of Balsara [14] and Balsara and Spicer [15] to clean the numerical monopole each step. Thus the solution is free from spurious $\nabla \cdot \boldsymbol{B}$.

3. Test problems

In this section we show two test computations. The first one is collision of expanding gas sphere and radial inflow, while the second one is the zigzagged shock wave. The former example is purely hydrodynamical and contains no magnetic fields. The solution is, however, obtained with the MHD code.

3.1. Spherical expansion

In this subsection we examine collision of an expanding gas sphere with radial inflow, i.e., a spherical explosion in an accreting flow. In this example, a strong spherical shock wave forms and propagates outward. This example is computed with the uniform grid having 128^3 cells. The initial density is $\rho = 16$ inside a unit sphere while it is $\rho = 1.4$ outside the sphere. The initial pressure is $P = 20$ inside the sphere and $P = 0.2$ outside the sphere, respectively. The initial radial velocity is $v_r = -2.25$ outside the sphere, while it is proportional to the radial distance from the center inside the sphere, and $v_r = r$. The cell width is taken to be $\Delta x = 3.356 \times 10^{-2}$. The initial condition is shown in Fig. 2 as a function of the radial distance from the center of the computation region.

When we follow the evolution with the Roe scheme, the simulation suffers from the carbuncle instability. Fig. 3 shows the stage 260 time steps after the initial. The contours denote the entropy, $s \equiv \ln P - (5/3)\ln\rho$, on the cross section of the mid ($z = 0$) plane. The lower panel is the enlargement of the upper one around the carbuncle.

Fig. 4 is the same as Fig. 3 but for the solution obtained with the modified numerical flux. The carbuncle has been removed as expected, although we can see irregularities in the contours. The irregularities result from using a cubical grid for a spherical problem. The initial radius is only 29.8 times larger than the cell width for the expanding sphere. The boundary between the expanding sphere and accreting flow depends on the resolution; a small change in the resolution results in appreciable changes in the shape of contours.

Next we examine the additional viscosity of the modified numerical flux. The fast mode, which is identical to the sound wave in this example, has no additional viscosity. The slow mode vanishes since the magnetic field vanishes. Thus, the additional numerical viscosity is supplemented only to the Alfvén wave (velocity shear) and entropy wave. Fig. 5 shows the additional numerical viscosity supplemented to the Alfvén wave, $\Lambda^{(2)} - \lambda^{(2)}$. The upper panel denotes that for the shear (Alfvén) wave propagating rightward in the x-direction by darkness, while the lower panel denotes that propagating rightward in the z-direction. They are evaluated on the mid plane of $z = 0$. The grey scale for the darkness is given on the top of the upper panel. The additional numerical viscosity is large around the two shock waves, one of which propagates outwards and the other of which does inwards. The viscosity is larger around the former shock wave, since it is stronger.

The amount of the additional numerical viscosity is also shown in Fig. 6. The ordinate is given in the unit of velocity. The ordinary numerical viscosity is the characteristic speed and hence of the order of flow velocity and sound speed. Since the expansion velocity is of the order of unity, the additional numerical viscosity is much lower than the ordinary numerical viscosity except near the shock fronts.

3.2. Odd–even test

We computed Quirk's [3] odd–even problem as a litmus test for the carbuncle instability with our 3D MHD code. The coordinates are chosen so that the shock front is normal to the x-direction and the wave number of the initial perturbation is parallel to the y-direction. Everything is constant in the z-direction at the initial state.

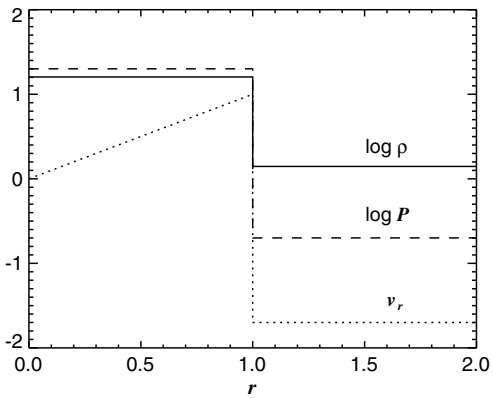

Fig. 2. Initial density, velocity, and pressure are shown as a function of the radius, r, for the spherical expansion test. The density and pressure are shown in the logarithmic scale while the velocity in the linear scale.

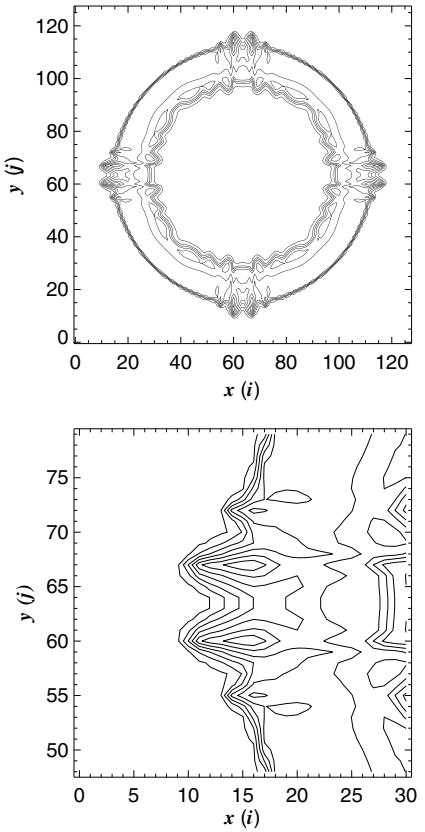

Fig. 3. Spherical expansion test solution without additional viscosity. The contours denote, $s = \ln P - (5/3)\ln\rho$ with the interval of $\Delta s = 0.3$. The abscissa and ordinate denote the cell numbers in the x- and y-directions, respectively.

The gas is assumed to be an ideal mono atomic one ($\gamma = 5/3$) in this test. The right hand side is the preshocked flow while the left hand side is the postshocked one. We made 6 models by changing the initial condition.

The shock front moves at the speed of $v_{\rm sh} = 1.0$ in the first 5 models. The strength of initial magnetic field is the main difference between them. The magnetic field is assumed to vanish in the first problem, while it is parallel to the flow, i.e., the x-direction in the second problem. The magnetic field is assumed to be perpendicular to the flow in the rest three problems.

In the first problem, the initial state is set to be state is set to be

$$\rho_{i,j,k} = 1.0, \tag{44}$$
$$P_{i,j,k} = 0.6, \tag{45}$$
$$v_{x,i,j,k} = -5.0, \tag{46}$$
$$v_{y,i,j,k} = 0.0, \tag{47}$$
$$v_{z,i,j,k} = 0.0, \tag{48}$$

in the right hand side of ($i \geqslant 30$), where i, j, and k denote the cell position in the x-, y-, and z-directions, respectively. It is set to be

$$\rho_{i,j,k} = 3.692, \tag{49}$$
$$P_{i,j,k} = 26.85, \tag{50}$$
$$v_{x,i,j,k} = -0.625, \tag{51}$$
$$v_{y,i,j,k} = 0.0, \tag{52}$$
$$v_{z,i,j,k} = 0.0, \tag{53}$$

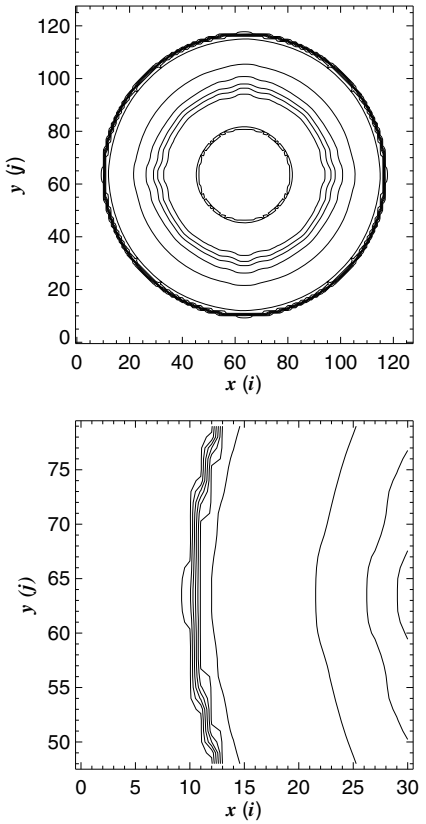

Fig. 4. The same as Fig. 3 but for the solution with the additional viscosity.

in the left hand side of $i \leqslant 29$. These states are arranged so that the boundary moves rightward at the phase velocity of 1.0 while keeping the initial density, velocity, and pressure. The shock Mach number is 6.0 in the preshocked (right) flow since the sound velocity is unity.

A small perturbation of $(\Delta\rho, \Delta P, \Delta v_x) = (-0.135, -1.31, 0.219)$ is added on the cells of an even j and $i = 29$. This small perturbation corresponds to 5% fluctuation in the wave front. Hence a zigzagged shock wave propagates rightward in the initial state. Fig. 7 shows the stage 100 and 200 time steps from the initial. The contours denote the distribution of specific entropy, s, on the x–y plane. No spatial dependence is seen in the z-direction. Since the solution is obtained without the additional viscosity, horizontal stripes are seen in the entropy distribution.

Fig. 8 is the same as Fig. 7 but for the solution obtained with the additional viscosity. The odd–even difference, $\Delta_y\rho \equiv \rho_{i,65,64} - \rho_{i,64,64}$, is erased out in Fig. 8. The density difference is at most $\Delta\rho = 3.0 \times 10^{-4}$ between two cells adjacent in the y-direction at this stage. This implies that the odd–even difference decreases by 6.1% per time step. In other words, it takes 37 time steps for the difference to decrease by a factor of 10.

The initial magnetic field is parallel to the x-axis ($B_x = 25$) in the second problem. The initial density, pressure, and velocity are the same as those in the first problem. Fig. 9 denotes the solution without the additional viscosity.

The odd–even difference neither grows nor dies out when the additional viscosity is not supplemented. The magnetic field parallel to the flow has an appreciable effect on the odd–even decoupling but does not suppress the odd–even difference. Note that the magnetic pressure is comparable to the gas pressure in the preshocked flow.

The odd–even difference was erased out in the simulation with the additional viscosity. Figs. 10–12 denote the odd–even differences in the solution with the additional numerical viscosity. The odd–even differences diminish while streaming downwards.

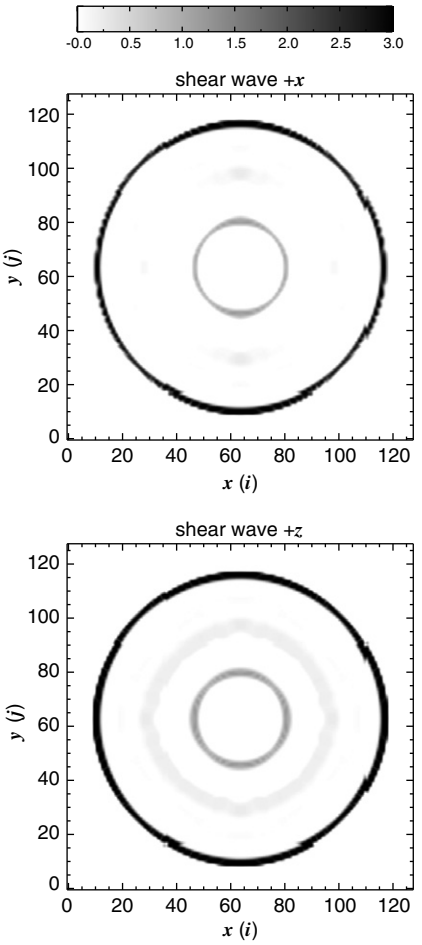

Fig. 5. The darkness denotes the additional numerical viscosity for spherical expansion, $\Lambda - |\lambda|$. The upper panel denotes that for the shear wave propagating rightward in the x-direction while the lower panel does that for propagating upward in the z-direction. It is evaluated in the plane of $z = 0$ and denoted in the unit of velocity.

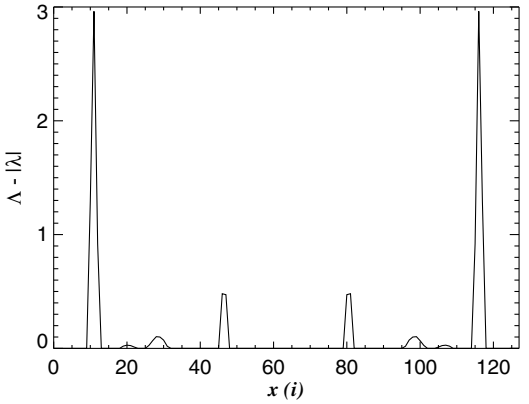

Fig. 6. The additional numerical viscosity is shown as a function of $x(i)$ on the line of $y = z = 0$ for the stage shown in Fig. 5. The solid curve denotes $\Lambda - |\lambda|$ for the shear wave propagating rightward in the x-direction while the dashed curve does that for the shear wave propagating in the right hand side in the z-direction.

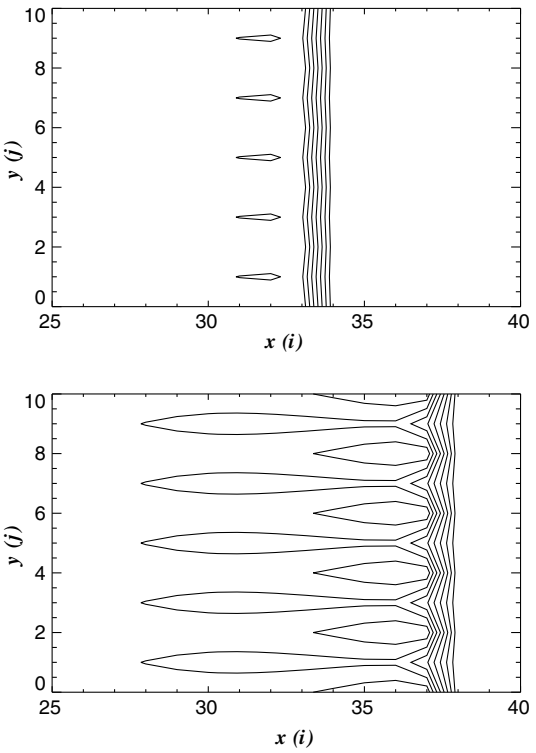

Fig. 7. Quirk's odd–even test problem solved without additional numerical viscosity. The curves denote the contours of $s \equiv \log P - \gamma \log \rho = 0.0, 1.0, 1.05, 1.10$, and 1.15 for the stages 100 (upper) and 200 (lower) time steps after the initial. The abscissa and ordinate denote the cell number in the x- and y-directions, respectively.

We assumed B_y, the magnetic field parallel to the shock front, in the third odd–even decoupling problem. The initial state in the right hand side was taken to be

$$\rho_{i,j,k} = 1.0, \tag{54}$$
$$P_{i,j,k} = 0.6, \tag{55}$$
$$v_{x,i,j,k} = -5.0, \tag{56}$$
$$v_{y,i,j,k} = 0.0, \tag{57}$$
$$v_{z,i,j,k} = 0.0, \tag{58}$$
$$B_{x,i,j,k} = 0.0, \tag{59}$$
$$B_{y,i,j,k} = 25.0, \tag{60}$$
$$B_{z,i,j,k} = 0.0, \tag{61}$$

while that in the left hand side was taken to be

$$\rho_{i,j,k} = 3.424, \tag{62}$$
$$P_{i,j,k} = 0.6, \tag{63}$$
$$v_{x,i,j,k} = -0.7523, \tag{64}$$
$$v_{y,i,j,k} = 0.0, \tag{65}$$
$$v_{z,i,j,k} = 0.0, \tag{66}$$
$$B_{x,i,j,k} = 0.0, \tag{67}$$
$$B_{y,i,j,k} = 13.30, \tag{68}$$
$$B_{z,i,j,k} = 0.0. \tag{69}$$

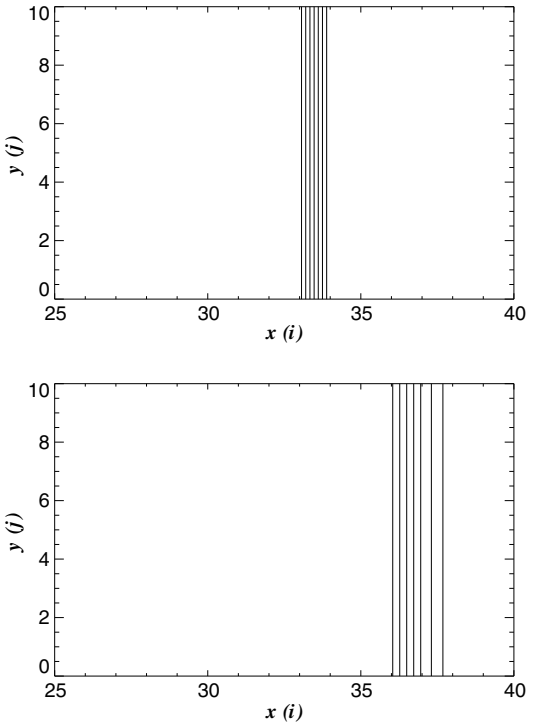

Fig. 8. The same as Fig. 7 but for the solution with the additional numerical viscosity.

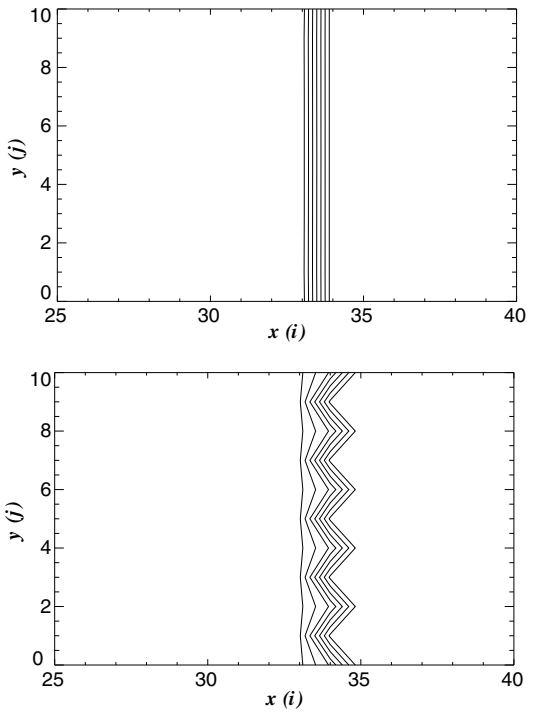

Fig. 9. The same as Fig. 7 but for the initial condition with B_x. The upper panel denotes the stage 200 steps after the initial while the lower does that 220 steps after the initial.

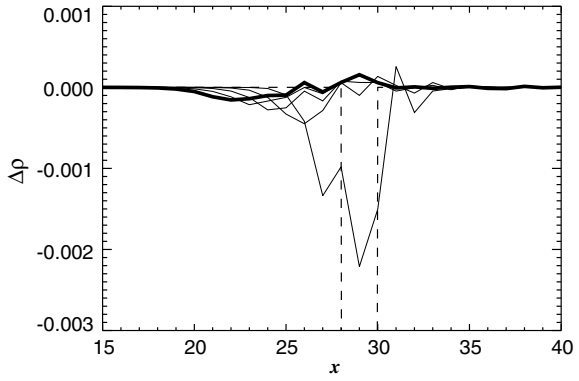

Fig. 10. The evolution of odd–even difference in the second problem when the additional numerical viscosity is supplemented. The lines denote the density difference in the cells adjacent in the y-direction, i.e., $\Delta_y\rho \equiv \rho_{i,65,64} - \rho_{i,64,64}$. The thin solid curves denote the stages of 20, 40, 60, and 80 time steps from the initial while the dashed curves do the initial stage. The thick solid curve does the stage 100 time steps from the initial. The abscissa denotes the x-coordinate in the cell number.

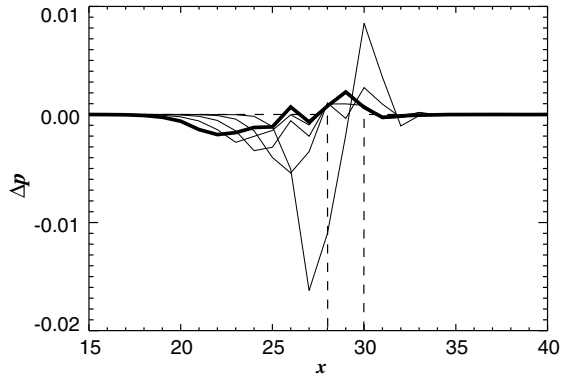

Fig. 11. The same as Fig. 10 but for the odd–even difference in pressure, $\Delta_y p$.

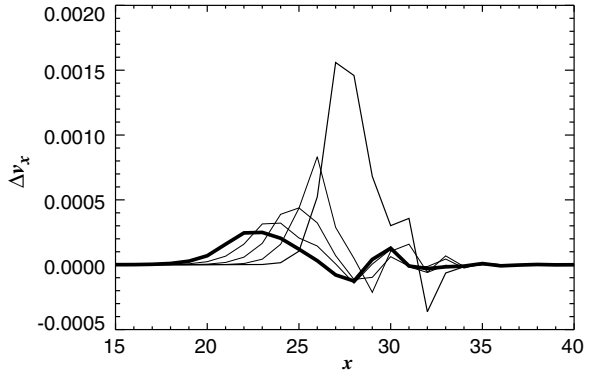

Fig. 12. The same as Fig. 10 but for the odd–even difference in the x-component of velocity, $\Delta_y v_x$.

This jump is arranged to propagate rightward at the phase velocity of 1.0. A small perturbation is added on the density, velocity, and pressure but not on the magnetic field. The odd–even decoupling was not observed in the third problem even in the simulation without the additional numerical viscosity. This is because the Alfvén wave propagates with an appreciable phase velocity in the y-direction. The Alfvén wave dissipates the difference in v_x through numerical diffusion.

We made the fourth odd–even problem from the third one by exchanging B_y and B_z. The odd–even decoupling grows in the fourth problem as shown in Fig. 13. The z-component of the magnetic field has no contribution to the diffusion in the y-direction. This carbuncle instability is also removed by the additional numerical viscosity.

From comparison of the second, third and fourth problems we have learned that the odd–even decoupling can be suppressed by the magnetic field but depending on the direction. When the perturbation is parallel to the magnetic field, it can be suppressed.

In order to understand the angle dependence, we examined the fifth problem in which the magnetic field is perpendicular to the flow and inclined with respect to the y- and z-axes, i.e., $\boldsymbol{B} \propto (0, 1/\sqrt{2}, 1/\sqrt{2})$ in the Cartesian coordinates. The initial density, velocity, and pressure are the same as those of the third and fourth problems. Also the initial amplitude of the magnetic field is the same as that of the third and fourth problems. The odd–even decoupling does not grow in the fifth problem. This implies that the odd–even decoupling is suppressed if the magnetic field has an appreciable component in the direction parallel to the perturbation. In other words, the odd–even decoupling and hence carbuncle instability will grow when the shock front is parallel to a coordinate and the magnetic field is parallel to another coordinate. Then the wave vector of unstable perturbation will be parallel to the rest coordinate.

Inspired by Kitamura et al. [4] we have added several models in which the shock front is stationary. The sixth model was constructed from the second model by subtracting $\Delta v_x = 1.0$ in the x-component of the velocity, i.e., $v_x = -6.0$ and -1.7523 in the left and right hand sides, respectively. The initial shock front was placed between $x = 119$ and 120. The initial density, and pressure, and magnetic field are the same as those in the second model.

The odd–even difference grows with the time in the sixth model when the Roe scheme with entropy fix is applied. The odd–even difference is damped when the additional numerical viscosity is supplemented. Fig. 14 denotes the evolution of the density difference between the cells adjacent in the y-direction in the computation with the additional numerical viscosity. The odd–even difference diminishes while streaming downward.

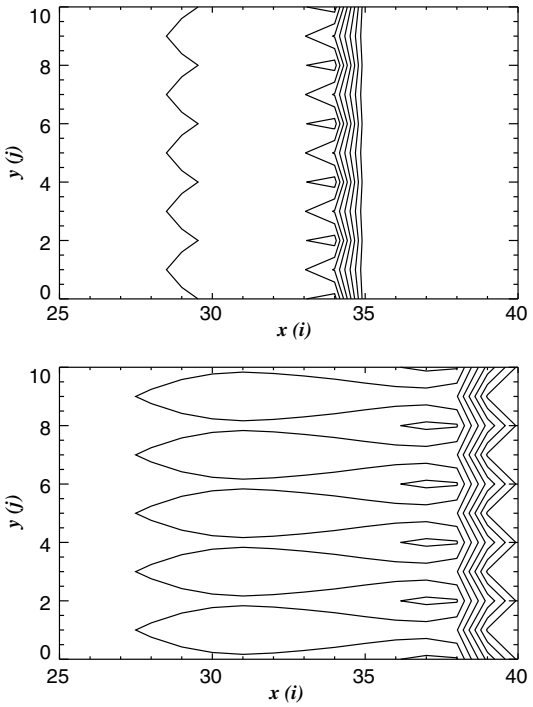

Fig. 13. The same as Fig. 7 but for the initial condition with B_z. The curves denote the contours of $s = 1.0$ and from 3.2 to 4.1 with 0.1 step. The upper and lower panels denote the stages of 100 and 200 time steps from the initial, respectively.

Figs. 15 and 16 are the same as Fig. 14 but for the odd–even differences in the pressure and x-component of the velocity. These differences diminish while streaming downward. No velocity perturbation is induced in the y-direction while the pressure varies along the y-axis. This is because the pressure perturbation has the wavelength only twice as long as the cell width. The velocity perturbation cannot be expressed since it should have a

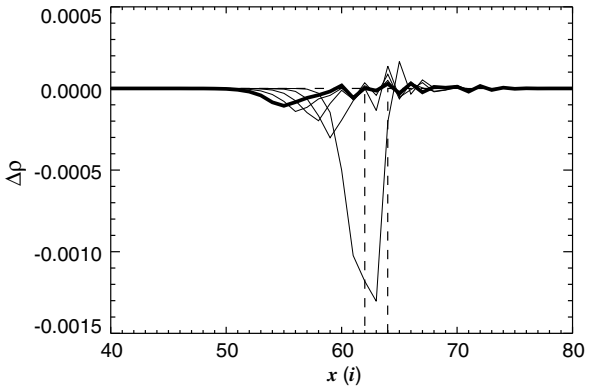

Fig. 14. The evolution of the odd–even difference when the shock front is stationary. The lines denote the density difference between the cells adjacent in the y-direction. The dashed line denotes that at the initial stage while the thick solid line does that at the stage time 100 steps from the initial. The thin solid lines denote those at the stages 20, 40, 60, and 80 time steps from the initial.

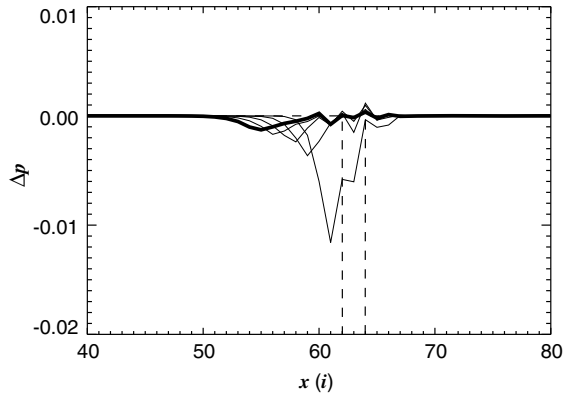

Fig. 15. The same as Fig. 14 but for the odd–even difference in the pressure.

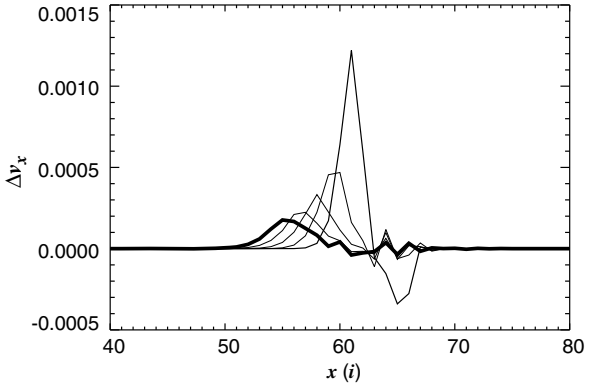

Fig. 16. The same as Fig. 14 but for the odd–even difference in the x-component of the velocity.

finite value on the cell surface but not at the cell center. In other words, a sound wave, a physical restoring process, cannot be expressed at such a short wave length. This may be related to a cause of the carbuncle instability.

Fig. 17 shows the density evolution in the above model. The curves denote the density profile as a function of x at fixed y and z. The density jump spreads over several cells after a few time steps. At the same time, sound wave and entropy wave are emitted from the jump to travel in the downstream.

Figs. 18 and 19 are the same as Fig. 14 but for the pressure (p) and velocity (v_x), respectively. Only the sound wave is seen in the pressure and velocity distributions.

We stopped the computation before the waves reach the boundary in the downstream since the density and velocity seemed to converge near the shock front. If we had continued the computation, the waves would be reflected between the boundary and shock front. The wave reflection would oscillate the shock front. The oscillation is the 1D carbuncle instability discussed by Kitamura et al. [4].

The reflection of the wave depends on the downstream boundary condition and also on the choice of the numerical scheme. The initial emission of the waves from the jump depends on the initial position of the shock front relative the cell boundary. As shown by Kitamura et al. [4], the condition for the 1D carbuncle instability is complex and beyond the scope of this study. It is further more difficult to track the shock front correctly in 2D and 3D stationary flows.

By computing several stationary shock flows, we have confirmed that the odd–even difference diminishes when our additional numerical viscosity is supplemented. The examples include the case in which the initial shock front is located inside a cell. Our numerical viscosity erases out the odd–even difference, while it may not care the 1D carbuncle instability.

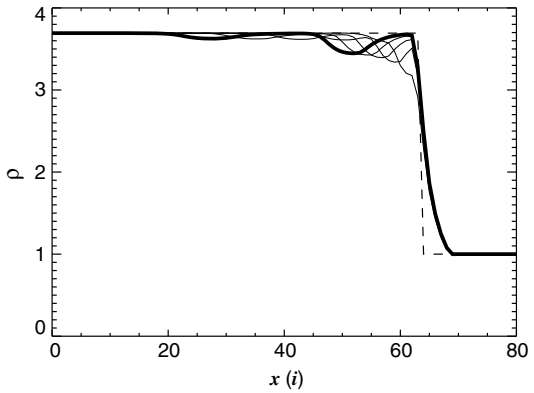

Fig. 17. The density evolution in a stationary shock problem. The dashed line denotes the initial state, while the solid curves denote those at the stages 100, 200, 300, 400, and 500 time steps from the initial.

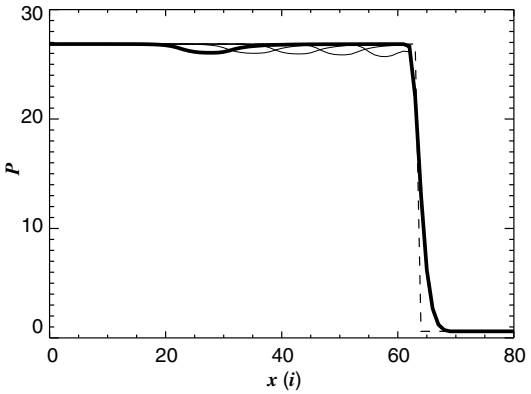

Fig. 18. The same as Fig. 17 but for the pressure evolution.

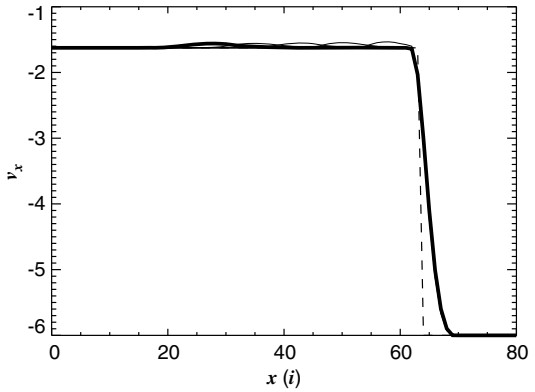

Fig. 19. The same as Fig. 17 but for the velocity evolution.

It should be noted that the Roe flux with entropy fix (Roe-Efix) has passed the 1D carbuncle test of Kitamura et al. [4]. Since entropy fix is commonly employed in the practical use, the 1D carbuncle instability is not likely to be serious to the computation obtained with the Roe flux.

4. Application to type II supernova

We applied our scheme to three-dimensional MHD simulation of type II supernova. Type II supernova is explosion taking place at the final evolutionary stage of a massive star. Just before the explosion, the central iron core of a massive star exceeds the critical mass and starts to collapse dynamically. Our numerical simulation deals with the collapse of the iron core and subsequent supernova explosion.

Our initial data are constructed based on the 15 $M_\odot$ model of Woosley et al. [17]. The density is increased 10% artificially to initiate the dynamical collapse. The initial magnetic field is assumed to be

$$\begin{pmatrix} B_r \\ B_\theta \\ B_\varphi \end{pmatrix} = \frac{2B_0}{3}(r_b - r_a)\begin{pmatrix} \cos\theta \\ \sin\theta \\ 0 \end{pmatrix} \tag{70}$$

in the central core of $r \leqslant r_a$,

$$\begin{pmatrix} B_r \\ B_\theta \\ B_\varphi \end{pmatrix} = \frac{B_0}{12}\begin{bmatrix} \left(8r_b + 6r + \frac{2r_a^4}{r^3}\right)\cos\theta \\ \left(8r_b + 3r + \frac{r_a^4}{r^3}\right)\sin\theta \\ 0 \end{bmatrix}, \tag{71}$$

in the middle region of $r_a \leqslant r \leqslant r_b$, and

$$\begin{pmatrix} B_r \\ B_\theta \\ B_\varphi \end{pmatrix} = \frac{B_0}{12}(r_b^4 - r_a^4)\begin{pmatrix} \cos\theta \\ \sin\theta \\ 0 \end{pmatrix} \tag{72}$$

in the outer region of $r_b \leqslant r$, in the spherical coordinates. The electric current density is uniform in the spherical shell of $r_a \leqslant r < r_b$ in this magnetic configuration.

The initial rotation velocity is expressed to be

$$\boldsymbol{v}_0 = \Omega(r)(\boldsymbol{e}_\Omega \times \boldsymbol{r}), \tag{73}$$

where

$$\Omega(r) = \frac{\Omega_0 a^2}{r^2 + a^2}, \tag{74}$$

$$\boldsymbol{e}_\Omega = \begin{pmatrix} \sin\theta_\Omega \\ 0 \\ \cos\theta_\Omega \end{pmatrix}, \tag{75}$$

and

$$\boldsymbol{r} = \begin{pmatrix} x \\ y \\ z \end{pmatrix}, \tag{76}$$

in the Cartesian coordinates. The rotation axis is inclined by θ_Ω from the z-axis, i.e., from the magnetic axis. We set $\theta_\Omega = \pi/3$ in the following example.

We used the equation of state of Takahara and Sato [16] in which the pressure is expressed as

$$P = P_\mathrm{c} + P_\mathrm{t}, \tag{77}$$

$$P_\mathrm{t} = \frac{\rho\varepsilon_\mathrm{t}}{\gamma_\mathrm{t} - 1}, \tag{78}$$

$$P_\mathrm{c} = K_i \left(\frac{\rho}{\rho_i}\right)^{\gamma_i}. \tag{79}$$

The index, γ_t, is taken to be 1.3. The coefficients, K_i and γ_i, are piecewise constant in the interval of $\rho_{i-1} < \rho \leqslant \rho_i$. The values are given in Table 1. The internal energy per unit mass is expressed as

$$\varepsilon = \varepsilon_t + \int_0^\rho \frac{P_\mathrm{c}}{\rho^2}\,\mathrm{d}\rho. \tag{80}$$

Table 1
Model parameters for P_c [see Eq. (79)]

i	ρ_i	K_i	γ_i
1	4.0×10^9	1.767×10^{27}	4/3
2	1.0×10^{12}	2.446×10^{30}	1.31
3	2.8×10^{14}	4.481×10^{33}	4/3
4	1.0×10^{15}	1.080×10^{35}	2.5

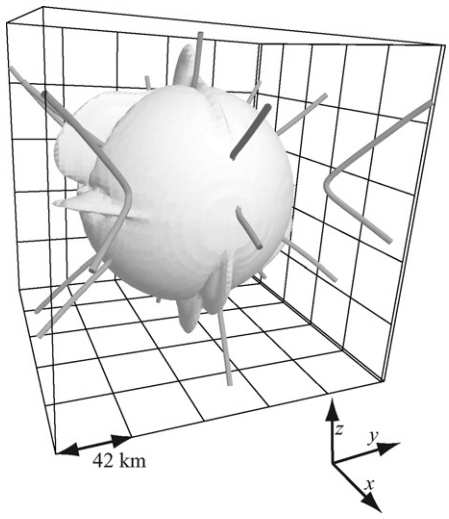

Fig. 20. Numerical simulation of a prompt shock wave from a proto neutron star. Painted is the surface of constant radial velocity, $v_r = 10^4$ km s^{-1}. Though the shock wave should be almost spherical, it suffers from the carbuncle instability.

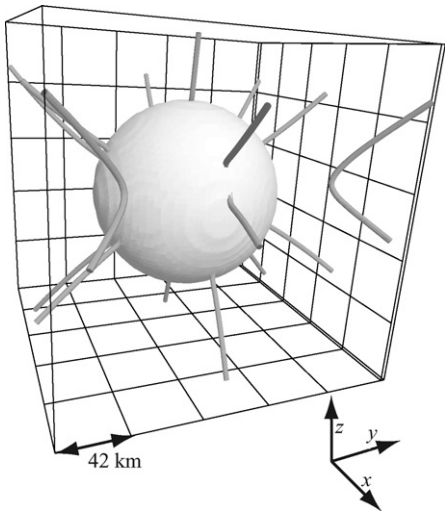

Fig. 21. The same as Fig. 20 but for the simulation with the additional numerical viscosity. The carbuncle instability is removed perfectly.

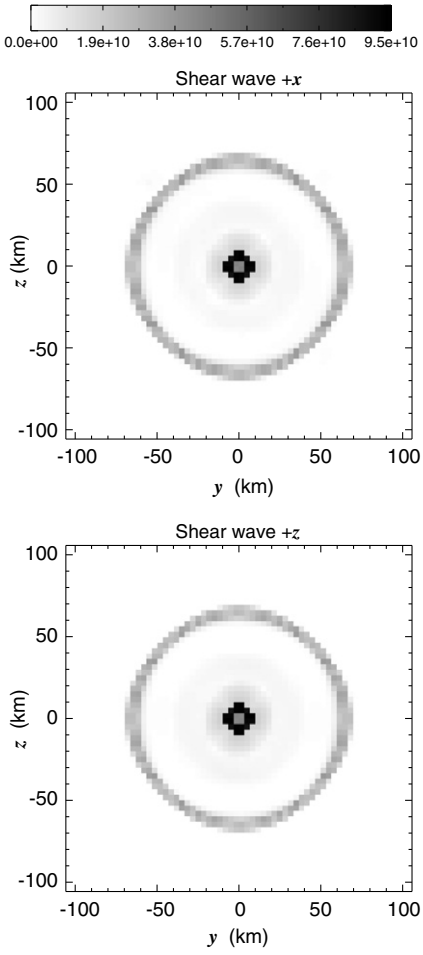

Fig. 22. The amount of additional numerical viscosity is denoted by grayness for the stage shown in Fig. 21. It is measured on the plane of $x = 1.65$ km in unit of velocity as described in the text. The upper panel denotes the additional numerical viscosity for the Alfvén wave propagating in the increasing x while the lower panel does that in the increasing z.

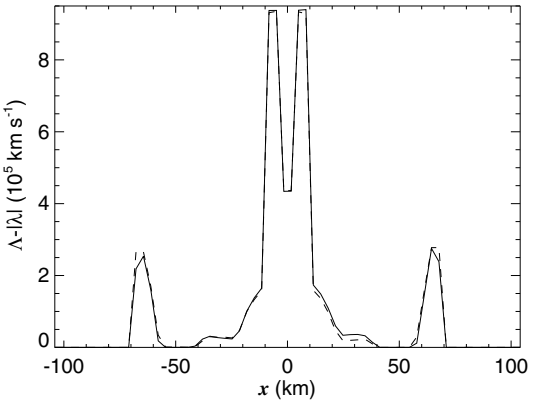

Fig. 23. The additional numerical viscosity, $\Lambda - |\lambda|$, is shown as a function of x for the stage shown in Fig. 22.

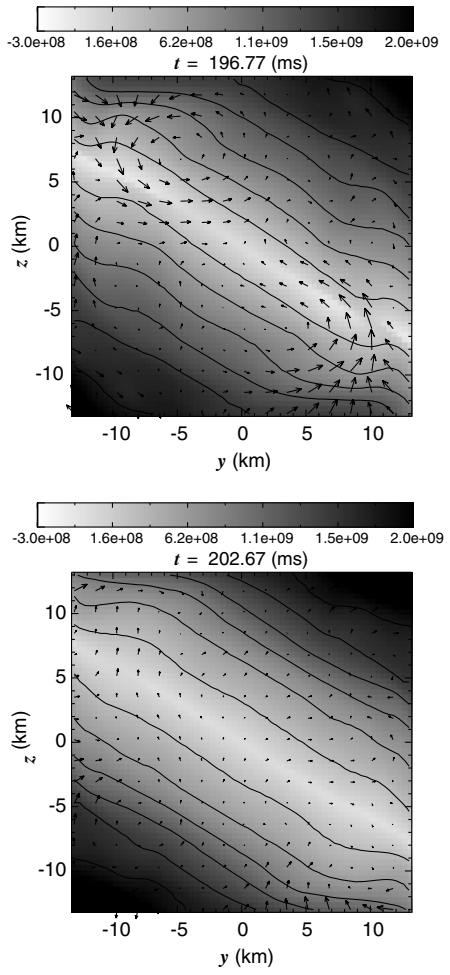

Fig. 24. The grayness denotes the rotation velocity, v_φ, around the initial rotation axis at the stages of $t = 196.77$ ms (upper) and 202.67 ms (lower). The arrows denote the velocity within the plane. This solution is obtained with the additional numerical viscosity to the Roe scheme.

The MHD equations are solved on the nested grids consisting of eight concentric cubic grids. Each cubic grid contains 64^3 cells of which size differs by factor two each. The coarsest grid covers the volume of $(3383\ \mathrm{km})^3$ with the resolution of $\Delta x = 52.8$ km while the finest grid covers the central volume of $26.4\ \mathrm{km}^3$ with $\Delta x = 413$ m. The gravity was obtained by solving the Poisson equation with the multi grid iteration [18].

Fig. 20 shows the stage of $t = 190.54$ ms by a bird's eye view. The tubes denote the magnetic field lines. Painted is the isovelocity surface of $v_r = 1.0 \times 10^4\ \mathrm{km\ s^{-1}}$ and corresponds to the expanding wave called the prompt shock. The prompt shock is formed by the bounce of collapsing stellar core, i.e., birth of a proto neutron star ($t = 189.83$ ms). The radius of the proto neutron star is about 10 km. The prompt shock wave emanates from the surface of the proto neutron star and its radius increases from 21.5 km to 73.5 km by the stage of $t = 190.38$ ms. Though the shock wave should be nearly spherical, it has bumps on the planes of $x = 0$, $y = 0$ and $z = 0$. They are due to the carbuncle instability since they are along the cell boundaries. At this stage the plasma beta is much higher than unity and the magnetic force is weaker than the gas pressure force.

Fig. 21 is the same as Fig. 20 but for the simulation with the additional viscosity. The carbuncle instability is removed completely and the shock front is fairly smooth.

Fig. 22 shows the amount of additional numerical viscosity for the Alfén waves, i.e., $\Lambda^{(m)} - |\lambda^{(m)}|$. It is evaluated on the plane of $x = 1.65$ km for the Alfvén wave propagating in the increasing x-direction (upper panel)

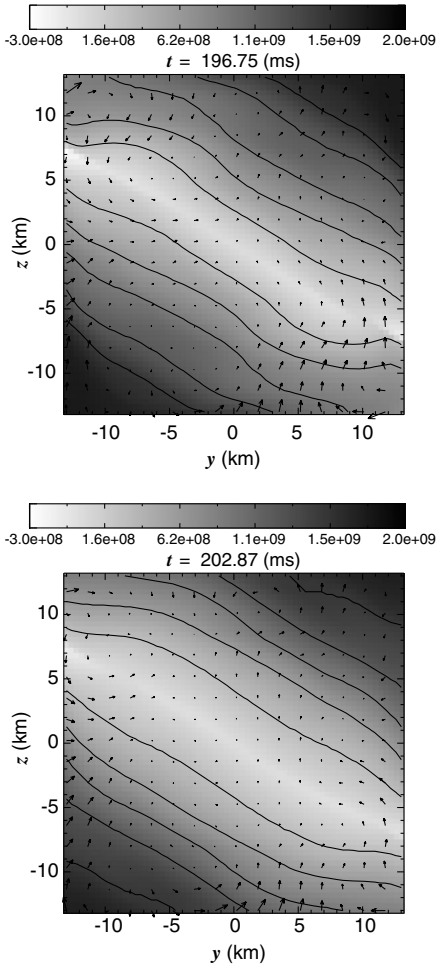

Fig. 25. The same as Fig. 24 but for the solution obtained with the HLLE scheme. The upper and lower panels denote the stages of $t = 196.75$ ms and 202.87 ms, respectively.

and that in the increasing z-direction (lower panel). The additional numerical viscosity is small except near the prompt shock and near the proto neutron star. See also Fig. 23 for the absolute value of the additional numerical viscosity.

Next we compare our scheme with the HLLE scheme [5,6] using this example. The HLLE scheme also solves the prompt shock without suffering from the carbuncle instability. The solution obtained with the HLLE scheme is smeared by numerical diffusion. In other words, the magnetic Reynolds number is decreased artificially. Fig. 24 shows the rotation velocity distribution in the solution obtained with our scheme while Fig. 25 does that with the HLLE scheme. The darkness denotes the rotation velocity on the plane of $x =$ 413 m. The arrows denote the velocity within the plane. The upper panels denote the stage of $t = 196.8$ ms while the lower ones do that of $t = 202.8$ ms. The initial rotation axis lies in the plane of $x = 0$ and is inclined with 60° from the z-axis. The rotation of proto neutron star, of which radius is about 10 km, is appreciably decreased in the solution obtained with HLLE. The maximum angular velocity is kept at the level of $\Omega \simeq 2 \times 10^3$ Hz in the simulation obtained with our scheme while it decreases in the HLLE simulation. The region of fast rotation is smaller in the HLLE simulation. This slow down is due to numerical diffusion of the HLLE scheme. The artificial slow down leads to serious loss of rotation energy in a supernova simulation.

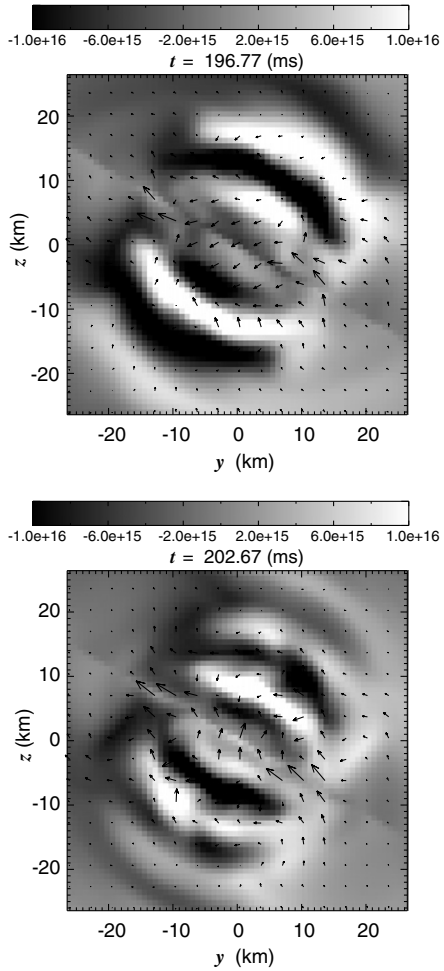

Fig. 26. Distribution of toroidal magnetic field generated by rotation of proto neutron star. The grayness denotes the toroidal component of the magnetic field (B_φ) around the initial rotation axis on the plane of $x = 206$ m. The arrows denote the magnetic field on the plane. The rotation velocities at the corresponding stages are shown in Fig. 24.

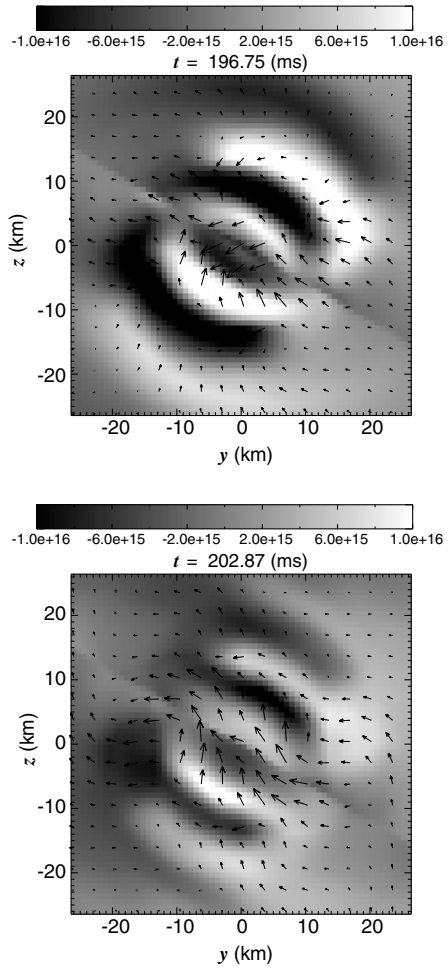

Fig. 27. The same as Fig. 26 but for the solution obtained with HLLE scheme. The rotation velocities at the corresponding stages are shown in Fig. 25.

Magnetic field is also smeared by numerical diffusion in the solution obtained with the HLLE scheme. Fig. 26 denotes the toroidal magnetic field (B_φ) distribution obtained with our scheme, while Fig. 27 does that obtained with the HLLE scheme. The toroidal magnetic field is small inside the proto neutron star in the solution obtained with our scheme while it is large in the solution obtained with the HLLE scheme. The difference comes from the large numerical viscosity of the HLLE scheme.

Fig. 28 denotes the magnetohydrodynamical jets launched from the proto neutron star. These jets are driven by the toroidal magnetic fields in the simulation with our scheme. These MHD jets are not launched in the simulation with the HLLE scheme. As shown here, too large numerical diffusion can be serious in 3D MHD simulations since spatial resolution is rather limited.

5. Discussion

As shown in the previous sections, our scheme has succeeded in solving the spherical expansion problem, Quirk's odd–even test, and MHD type II supernova explosion. The former two tests prove that the additional numerical viscosity can save the carbuncle instability and odd–even decoupling. The latter test proves that our scheme can be applied to an MHD flow associated with strong shock waves. It also demonstrates that the numerical viscosity of our scheme is appreciably smaller than that of HLLE.

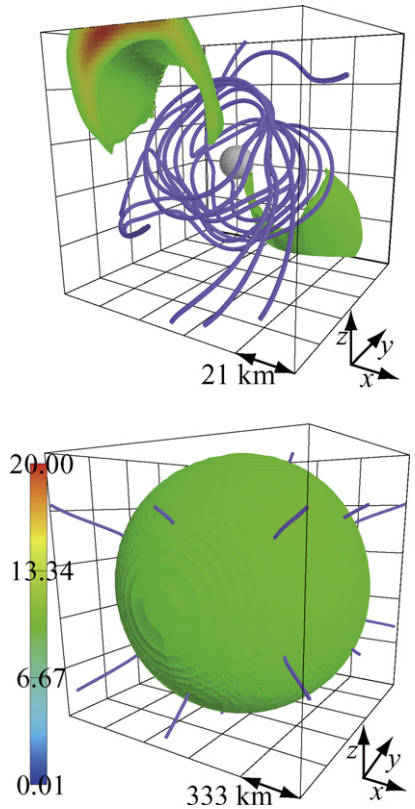

Fig. 28. Magnetohydrodynamical jets launched from rotating magnetized proto neutron star. Each panel denotes the stage of $t = 228.99$ ms by a bird's eye view. The upper and lower panels denote the central volumes of $(104\ \mathrm{km})^3$, and $(1665\ \mathrm{km})^3$, respectively. The purple curves denote the magnetic field lines while the color denotes the radial velocity, v_r, in the unit of $10^3\ \mathrm{km\ s^{-1}}$. The color scale is attached to the lower panel.

Our scheme has several advantages among the schemes free from the carbuncle instabilities. First it can be applied to magnetohydrodynamical equations while the other schemes except HLLE have not yet been applied. It can be applied to any hyperbolic equations. Second the numerical viscosity is much smaller than that of HLLE and as small as the Roe-type scheme except near the shock fronts. Third the shock indicator has the dimension of velocity as well as the additional numerical viscosity. Thus, the functional form of the numerical viscosity is simple in our scheme. Another advantage is implication of the mechanism for the carbuncle instability. Our scheme implies that the carbuncle instability is due to the convergence of waves at the shock fronts.

We suppose that the carbuncle instability is induced by the following mechanism working near the shock front. First a shock wave tends to confine any perturbation near the front through nonlinear interactions of waves. Remember that both sides are upstream from the shock front. Since information travels from upstream to downstream, no perturbation escapes in the direction normal to the shock front. Thus the perturbation remains in a small region near the shock front. Second the perturbation cannot travel in the direction tangential to the shock front if its wavelength is as small as twice the cell width. As demonstrated by the odd–even test, a velocity perturbation decouples from density and pressure perturbations at such a short wavelength. No velocity perturbation tangential to the shock front is induced in the sample problem shown in Fig. 7.

In our scheme a perturbation near the shock front is dispersed in the tangential direction through the artificial viscosity. The viscosity is proportional to the convergence rate of the characteristics, $\Delta\lambda$, for the Alfvén and slow waves, while it is larger for the entropy wave. We have tried the same numerical viscosity for the entropy wave but failed. Our experience means that a larger numerical viscosity is required for the entropy wave to suppress the carbuncle instability. We suppose that the Alfvén and slow waves are amplified through

a passive nonlinear coupling, while the entropy wave is amplified through a stronger nonlinear coupling, i.e., entropy generation at the shock front.

Though our scheme has succeeded in suppressing the carbuncle instability in a problem of our interest, its applicability has been explored a little. It is partly because the mechanism of the carbuncle instability has not been clearly understood. Exploration of the applicability has no alternative but application to various test problems. For robustness we need to examine various cell widths, since the carbuncle instability is sensitive to them. Thus the approach cannot help being phenomenological. In order to explore the robustness, we need to identify the mechanism. We hope that our approach based on the characteristics contributes to full understanding of the carbuncle instability.

Numerical examples are performed in part on SR11000 at the Institute of Media and Information Technology of Chiba University. This work is financially supported in part by the Grant-in-Aid for Priority Area by the Ministry of Education, Culture, Sports, Science and Technology (17030002).

References

[1] K.M. Peery, S.T. Imlay, Blunt-body flow simulations, AIAA Paper 88-2904, 1988.
[2] P.L. Roe, Approximate Riemann solvers, parameter vectors, and difference schemes, J. Comput. Phys. 43 (1981) 357.
[3] J.J. Quirk, A contribution to the great Riemann solver debate, Int. J. Numer. Methods Fluids 18 (1994) 555.
[4] K. Kitamura, P. Roe, F. Ismail, An evaluation of Euler fluxes for hypersonic flow computations, in: 18th AIAA Computational Fluid Dynamics Conference, 2007, AIAA 2007-4465.
[5] A. Harten, P.D. Lax, B. van Leer, On upstream differencing and Godunov-type schemes for hyperbolic conservation laws, SIAM Rev. 25 (1983) 35.
[6] B. Einfeldt, On Godunov-type methods for gas dynamics, SIAM Numer. Anal. 25 (1988) 294.
[7] Y. Wada, M.-S. Liou, An accurate and robust flux splitting scheme for shock and contact discontinuities, SIAM J. Sci. Comput. 18 (1997) 633.
[8] S.-S. Kim, C. Kim, O.-H. Rho, S.K. Hong, Cures for the shock instability: development of a shock stable Roe scheme, J. Comput. Phys. 185 (2003) 342.
[9] M.-S. Liou, Mass flux scheme to connection to shock instability, J. Comput. Phys. 160 (2000) 623.
[10] M. Brio, C.C. Wu, An upwind differencing scheme for the equations of ideal magnetohydrodynamics, J. Comput. Phys. 75 (1988) 400.
[11] P. Cargo, G. Gallice, Roe matrices for ideal MHD and systematic construction of Roe matrices for systems of conservation laws, J. Comput. Phys. 136 (1997) 446.
[12] T. Hanawa, H. Mikami, Y. Sato, T. Matsumoto, An approximate Riemann solver for the MHD equations and its application to type II supernova, in: Numerical Modeling of Space Plasma Flows ASTRONUM-2006, N.V. Pogorelov, G.P. Zank, (Eds.), ASP Conference Series, vol. 359, 2006, p. 158.
[13] C.Hirsch, Hirsch, Numerical Computation of Internal and External Flows, vol. 2, Wiley, Chichester, 1992, Chapter 21.
[14] D. Balsara, Divergence-free adaptive mesh refinement for magnetohydrodynamics, J. Comput. Phys. 174 (2001) 614.
[15] D. Balsara, D. Spicer, A staggered mesh algorithm using high order Godunov fluxes to ensure solenoidal magnetic fields in magnetohydrodynamic simulation, J. Comput. Phys. 149 (1999) 270.
[16] M. Takahara, K. Sato, Effects of neutrino trapping on supernova explosions, Prog. Theor. Phys. 68 (1982) 795.
[17] S.E. Woosley, A. Heger, T.A. Weaver, The evolution and explosion of massive stars, 1015 Rev. Mod. Phys. 74 (2002) 1015.
[18] T. Matsumoto, T. Hanawa, A fast algorithm for solving the Poisson equation on a nested grid, Astrophys. J. 583 (2003) 296.